Heat transfer characteristics of supercritical water in a tube: Application for 2D and an experimental validation

Jan A.M. Withag [a,*], Joost L.H.P. Sallevelt [a], Derk W.F. Brilman [b], Eddy A. Bramer [a], Gerrit Brem [a]

[a] University of Twente, Department of Thermal Engineering, Faculty of Engineering Technology, Drienerlolaan 5, 7500 AE Enschede, The Netherlands
[b] University of Twente, Thermo-chemical Conversion of Biomass (TCCB), Faculty of Science and Technology, Drienerlolaan 5, 7500 AE Enschede, The Netherlands

ABSTRACT

Heat transfer to water at supercritical pressures has been numerically investigated using a two-dimensional modeling approach. The simulations in a two-dimensional domain have been performed using the low-Reynolds k–ϵ turbulence model, and the IAPWS-IF97 formulation to describe the properties of water at different conditions.

The accuracy of the model is validated using an experimental setup at supercritical pressures. The experimental dataset was obtained in supercritical water flowing upward in a 0.4 m long vertical bare tube with 10 mm ID. The temperature data were collected at multiple heights in the tube and at pressures of about 24 MPa, an inlet temperature of 300 °C, values of mass flux ranged from 6.6 to 10 kg/m^2 s and an outer wall temperature of 300 °C resulting in bulk-fluid temperatures exceeding the pseudo-critical temperature. The comparison of the temperature results shows a good agreement for low mass fluxes between the experimental and numerical data. At these low flow conditions, the 2D model predicts recirculation zones near the inlet which results in a more complex simulation. The accuracy of the 2D model for higher fluxes cannot be properly assessed on basis of the experimental data because of practical limitation of the setup. But the accuracy of the 2D model for the higher mass flow cases is expected to be even more accurate, due to less complexity in the flow calculation because of smaller buoyancy effects.

Finally simulation results of the two-dimensional model at higher mass flows are compared with several frequently used one-dimensional correlations from literature for heat transfer at supercritical pressures.

© 2012 Published by Elsevier B.V.

1. Introduction

Water is in the supercritical state when both the pressure and the temperature are higher than the critical pressure and critical temperature (P_{cr} = 22.064 MPa and T_{cr} = 373.95 °C). The physical properties of supercritical water strongly differ from liquid water or steam. Supercritical water has much lower values for the dielectric constant, the viscosity, the thermal conductivity and in the vicinity of the critical point a large peak in the specific heat capacity can be detected [1,2].

Supercritical water is of great interest for several applications such as supercritical water gasification or supercritical water cooled-nuclear reactors. Supercritical water gasification is a challenging thermo-chemical conversion route for wet biomass and waste streams into valuable product gases, rich in either hydrogen or methane. Whereas supercritical water cooled reactors use the thermal properties of supercritical water to increase the thermal efficiency. Both application fields want to use the unique properties of supercritical water in order to optimize the process. For this purpose good prediction methods for the transport phenomena present in the reactor or heat exchanger are of great importance.

To predict the properties of water at different conditions the IAPWS-IF97 formulation [3] is used in this research. The IAPWS-IF97 formulation consists of a set of equations from which thermo-physical properties such as specific volume, enthalpy, thermal conductivity, viscosity and heat capacity can be derived. A detailed description of the IAPWS-I97 formulation can be found in the work of Sallevelt et al. [4] and the work of Wagner et al. [3].

Sallevelt et al. [4] describe a one-dimensional heat transfer model to simulate a supercritical water flow in a tube. With the use of the one-dimensional model various Nusselt correlations found in literature describing the heat transfer are compared. The results for the different Nusselt correlations show large deviations, which indicates that the used correlations have only limited applicability. Therefore in this work a 2D simulation is developed to investigate the influence of two-dimensional effects on the flow and heat transfer in supercritical water.
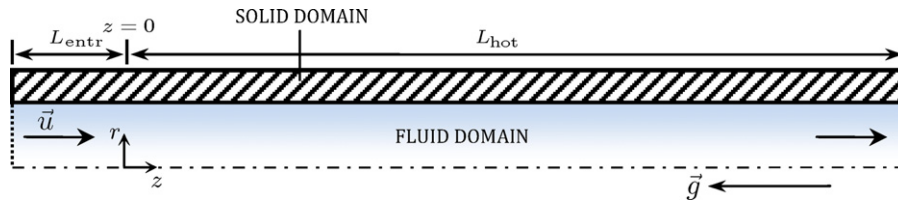
Fig. 1. Computational domain for the 2D model.

In the present study a two-dimensional model has been developed using the low-Reynolds k–ϵ turbulence model and the IAPWS-IF97 formulation. Furthermore, an experimental setup has been built to measure the heat transfer in supercritical water. Model results have been validated against experimental data for different mass fluxes. Finally, a comparison with the one-dimensional simulation results as obtained by Sallevelt et al. [4] is made to investigate the loss of accuracy due to the numerous simplifications made for the one-dimensional model. The calculations under investigation in this research have been performed using the software package COMSOL Multiphysics, which provides an advanced solver that is able to handle the two-dimensional model equations.

2. Computational domain

Assuming the problem is axi-symmetric around the centerline of the pipe, the entire pipe flow is covered by choosing half a cross-section as the computational domain. The computational domain includes the pipe wall and is shown in Fig. 1, drawn horizontally for a compact view. The heated section of the pipe L_{hot} is preceded by an entrance section L_{entr} with a length of 0.1 m for the development of the hydrodynamic boundary layer.

The domains are meshed using second order Lagrange elements. The fluid domain is covered by a structured grid of quadrilateral elements, while triangular elements are used for the solid domain in order to achieve a fast transition to a coarse mesh. A boundary layer mesh consisting of slender quadrilaterals is added to the fluid domain to cope with the high gradients in the boundary layer. A mesh convergence study is carried out to check whether the mesh satisfactorily balances accuracy and computing resources.

Data for the convergence analysis has been generated by simulating a case at 240 bar, a wall temperature of 600 °C and a mass flux of 20 kg/m² s. This in done in a tube with an inner diameter of 10 mm using the gridsizes shown in Table 1.

The surface-averaged density, temperature and isobaric heat capacity at the outlet are chosen as indicators for the mesh convergence. The results have been normalized and plotted in Fig. 2 together with a quadratic curve fit.

Although the convergence analysis calls for one of the finest meshes, a gridsize of 0.2 mm was adopted for the full pipe length of 2.5 m because a finer mesh would require more memory resources than available. Fig. 2 shows that the calculated heat capacity at the outlet is still significantly affected by the gridsize at this point. However, more important is the convergence of the density and

Table 1
Gridsizes and corresponding total number of elements used for the 2D mesh convergence analysis.

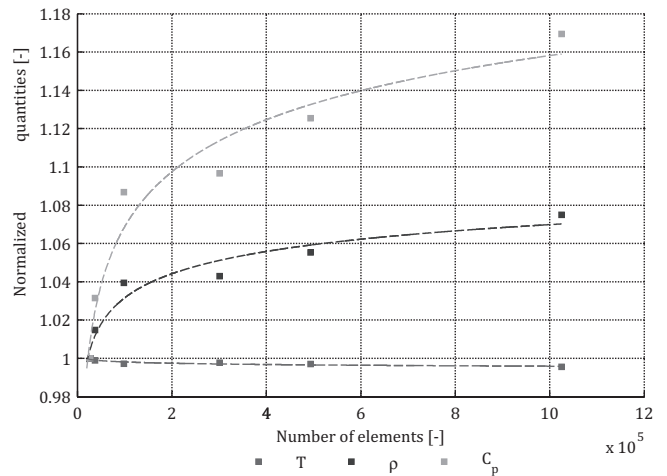| Gridsize	Number of elements (–)
0.5	27,530
0.4	37,660
0.2	98,692
0.1	300,964
0.075	494,038
0.05	1,025,210

Fig. 2. Mesh convergence for the 2D model on basis of normalized, surface-averaged quantities at the outlet. The data points shown correspond to gridsizes of 0.5, 0.4, 0.2, 0.1, 0.075 and 0.05 mm.

temperature, which is acceptable for the chosen gridsize. The practical limitation of the number of elements will for this reason not necessarily lead to inaccurate results.

By choosing 0.2 mm as the element size for the structured mesh covering the fluid domain, the complete mesh consists of 700,717 elements (585,000 quadrilateral and 115,717 triangular). To give an impression, this mesh is shown in Fig. 3 for a length of 10 mm.

3. 2D model equations

This section describes the equations for steady, compressible, two-dimensional flow. For this type of flow, the continuity equation
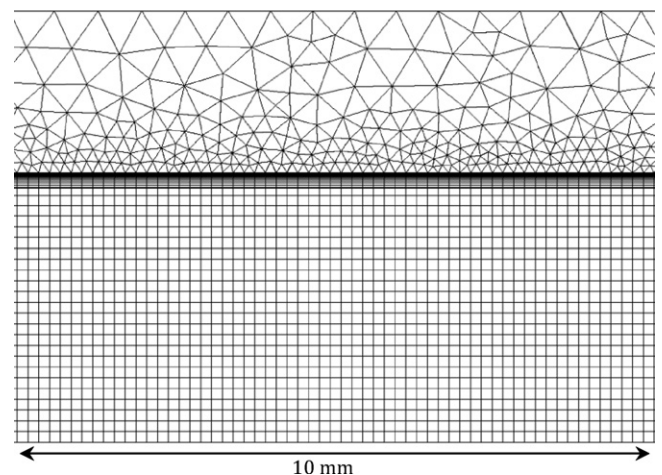

Fig. 3. Mesh for a 10 mm section of the 2D computational domain.

is obtained by neglecting the time-dependent term in continuity of mass equation, which results in:

$$\vec{\nabla} \cdot (\rho \vec{u}) = 0. \tag{1}$$

The steady state formulation of the momentum equation reads:

$$\rho(\vec{u} \cdot \vec{\nabla})\vec{u} = -\vec{\nabla}p - \vec{\nabla} \cdot \vec{\vec{\tau}} + \rho\vec{f} \tag{2}$$

where the viscous stress tensor is prescribed by Newton's law of viscosity:

$$\vec{\vec{\tau}} = -\mu(\vec{\nabla}\vec{u} + (\vec{\nabla}\vec{u})^T) + \frac{2}{3}\mu(\vec{\nabla} \cdot \vec{u})\vec{\vec{\delta}}. \tag{3}$$

The volumetric force vector accounts for the gravity force that acts downward in z-direction:

$$\vec{f} = \begin{Bmatrix} f_r \\ f_z \end{Bmatrix} = \begin{Bmatrix} 0 \\ -g \end{Bmatrix}. \tag{4}$$

Conservation of energy is described by the equation of change for temperature, without the terms that represent pressure work and viscous heating. These simplifications are considered reasonable since no large pressure gradients will occur inside the reactor, and the heat generated by viscous effects will be negligible compared to the heat that is transferred through the pipe wall. Expanding the material derivatives and disregarding the time-dependent terms in this expression leads to:

$$\rho C_p(\vec{u} \cdot \vec{\nabla})T = \dot{Q} - \vec{\nabla} \cdot \vec{q} \tag{5}$$

where the heat flux is given by Fourier's law,:

$$\vec{q} = -k\vec{\nabla}T.$$

The heat source term $\dot{Q}$ is zero for heat transfer analysis, but could be used to include heat effects due to for example chemical reactions.

4. Turbulence modeling

The time-dependent chaotic behavior in the fluid flow occurs at a wide range of time and length scales. Although turbulence is in principle fully described by the Navier–Stokes equations, a huge number of elements are required to capture the smaller scales in the flow. For this reason, the small scales are modeled using a turbulence model, while the Navier–Stokes equations are solved for the averaged variables.

The turbulence model chosen for the 2D reactor simulations is the low-Reynolds number k–ϵ turbulence model [5]. In comparison to the standard k–ϵ turbulence model, the low-Reynolds formulation provides equations for resolving regions of slow flow (close to walls) far better. Though computationally more expensive, the low-Reynolds model should be used in models where the effects of walls are important. This is certainly the case for the non-isothermal flow in the reactor, where large property variations occur in the boundary layer and the heat flux at solid–liquid interface highly affects the final solution. The superiority over the standard k–ϵ turbulence model has been confirmed in literature [6].

While Reynolds-averaging is applied for incompressible flows, resulting in the well-known Reynolds averaged Navier–Stokes equations (RANS), a more convenient method for compressible flow is Favre averaging. The Favre averaging method is density-based to suppress terms involving density fluctuations. Variables are decomposed into an averaged component, indicated with a tilde (˜), and a fluctuating component, indicated with a double prime (″):
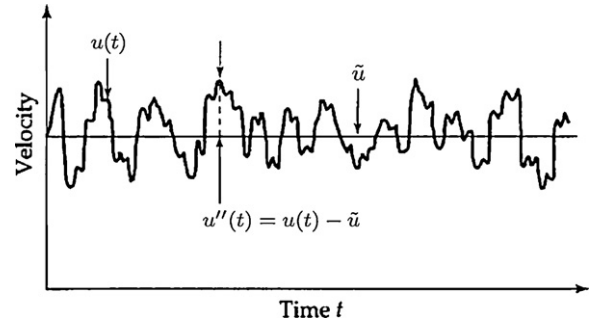
$$\phi = \tilde{\phi} + \phi'' \tag{6}$$

Fig. 4. Sketch showing the velocity component u as well as its smoothed value $\tilde{u}$ and its fluctuation u'' in turbulent flow for "steadily driven turbulent flow" in which $\tilde{u}$ does not depend on time [7].

where the averaged component is defined by:

$$\tilde{\phi} = \frac{1}{\overline{\rho}} \lim_{t_0 \to \infty} \frac{1}{t_0} \int_t^{t+t_0} \rho(\vec{x}, \tau)\phi(\vec{x}, \tau)d\tau. \tag{7}$$

This concept is illustrated in Fig. 4, where the velocity component $u(t)$ in "steadily driven turbulent flow" is decomposed into the averaged value $\tilde{u}$ and its fluctuation $u''(t)$.

When Favre averaging is applied to the model equations, Eqs. (1), (2) and (5) become:

$$\vec{\nabla} \cdot (\overline{\rho}\tilde{\vec{u}}) = 0 \tag{8}$$

$$\overline{\rho}(\tilde{\vec{u}} \cdot \vec{\nabla})\tilde{\vec{u}} = -\vec{\nabla}\tilde{p} - \vec{\nabla} \cdot (\tilde{\vec{\vec{\tau}}} + \tilde{\vec{\vec{\tau}}}_T) + \overline{\rho}\vec{f} \tag{9}$$

$$\overline{\rho}C_p(\tilde{\vec{u}} \cdot \vec{\nabla})\tilde{T} = \dot{Q} - \vec{\nabla} \cdot (\tilde{\vec{q}} + \tilde{\vec{q}}_T). \tag{10}$$

Here $\tilde{\vec{\vec{\tau}}}$ is the Favre averaged viscous stress tensor:

$$\tilde{\vec{\vec{\tau}}} = -\mu(\vec{\nabla}\tilde{\vec{u}} + (\vec{\nabla}\tilde{\vec{u}})^T) + \frac{2}{3}\mu\left(\vec{\nabla} \cdot \tilde{\vec{u}}\right)\vec{\vec{\delta}} \tag{11}$$

and $\tilde{\vec{\vec{\tau}}}_T$ is the Favre-averaged Reynolds stress tensor, which is modeled according to the turbulent viscosity hypothesis:

$$\tilde{\vec{\vec{\tau}}}_T = \overline{\rho\vec{u}''\vec{u}''} \tag{12}$$

$$= -\mu_T(\vec{\nabla}\tilde{\vec{u}} + (\vec{\nabla}\tilde{\vec{u}})^T) + \frac{2}{3}(\mu_T(\vec{\nabla} \cdot \tilde{\vec{u}}) + \overline{\rho}k)\vec{\vec{\delta}}.$$

Transport equations for the turbulent kinetic energy, k, and the turbulent energy dissipation rate, ϵ, are as follows:

$$\rho\frac{\partial k}{\partial t} + \rho\vec{u} \cdot \vec{\nabla}k = \vec{\nabla} \cdot [(\mu + \frac{\mu_T}{\sigma_k})\vec{\nabla}k] + P_k - \rho\epsilon \tag{13}$$

$$\rho\frac{\partial \epsilon}{\partial t} + \rho\vec{u} \cdot \vec{\nabla}\epsilon = \vec{\nabla} \cdot [(\mu + \frac{\mu_T}{\sigma_\epsilon})\vec{\nabla}\epsilon] + C_{\epsilon 1}\frac{\epsilon}{k}P_k - f_\epsilon C_{\epsilon 2}\rho\frac{\epsilon^2}{k} \tag{14}$$

with the auxiliary equations:

$$P_k = \mu_T\left[\vec{\nabla}\vec{u} : (\vec{\nabla}\vec{u} + (\vec{\nabla}\vec{u})^T) - \frac{2}{3}(\vec{\nabla} \cdot \vec{u})^2\right] - \frac{2}{3}\rho k(\vec{\nabla} \cdot \vec{u}) \tag{15}$$

$$\mu_T = \rho f_\mu C_\mu \frac{k^2}{\epsilon} \tag{16}$$

$$f_\mu = (1 - \exp^{-l^*/14})^2 \left(1 + \frac{5}{R_t^{3/4}}\exp^{-(R_t/200)^2}\right) \tag{17}$$

$$f_\epsilon = (1 - \exp^{-l^*/3.1})^2(1 - 0.3\exp^{-(R_t/200)^2}) \tag{18}$$

$$l^* = \frac{\rho u_\epsilon l_w}{\mu}, \quad R_t = \frac{\rho k^2}{\mu\epsilon}, \quad u_\epsilon = \left(\frac{\mu\epsilon}{\rho}\right)^2 \tag{19}$$

and the tuning coefficients are given by:

$$C_{\epsilon 1} = 1.5, \quad C_{\epsilon 2} = 1.9, \quad C_\mu = 0.09, \quad \sigma_k = 1.4, \quad \sigma_\epsilon = 1.5. \tag{20}$$

The parameter l_w in Eq. (19) is the distance to the closest wall, used by the turbulence model for regularization purposes or to approximate the mixing length. It is determined by solving the modified Eikonal equation [8]:

$$\vec{\nabla}\Lambda \cdot \vec{\nabla}\Lambda + \sigma_w \Lambda (\vec{\nabla} \cdot \vec{\nabla}\Lambda) = (1 + 2\sigma_w)\Lambda^4 \qquad (21)$$

where $\Lambda \equiv 1/l_w$ and σ_w is a small constant by default set to 0.1.

The heat transport turbulence model of Kays–Crawford [9] is used to model the turbulent heat flux in Eq. (10). The influence of the turbulent fluctuations on the temperature field is taken into account by adding a turbulent contribution to the thermal conductivity of the fluid:

$$\tilde{\vec{q}} + \tilde{\vec{q}}_T = -(k + k_T)\vec{\nabla}T \qquad (22)$$

where k is the thermal conductivity of the fluid and k_T is calculated from an expression for the turbulent Prandtl number:

$$\Pr_T = \frac{C_p \mu_T}{k_T}$$
$$= \left[\frac{1}{2\Pr_{T\infty}} + \frac{0.3}{\sqrt{\Pr_{T\infty}}} \frac{C_p \eta_T}{k} - \left(0.3 \frac{C_p \eta_T}{k} \right)^2 (1 - \exp^{-k/(0.3 C_p \eta_T \sqrt{\Pr_{T\infty}})}) \right]^{-1} . \quad (23)$$

Here the turbulent Prandtl number at infinity $\Pr_{T\infty}$ is experimentally determined to be 0.85 and the turbulent viscosity μ_T is given by Eq. (19). This model has been compared to other models for $\Pr_T$ and found to be good for most kind of turbulent wall bounded flows except for liquid metals [9].

5. Solving the 2D model equations

The 2D model equations have been solved on a linux-based computer cluster using the software package COMSOL Multiphysics (v4.1). The solution has been calculated on 1 node, each node consists of two quadcore Xeon E5620 processors running at 2.40 GHz and 24 GB of memory. The solving process took several hours using a direct solver. Direct solvers use more memory than iterative solvers, but are more robust and suitable for highly non-linear and multiphysics problems. Since the equations governing fluid flow and convective heat transfer are numerically unstable by nature, stabilization techniques have been applied to dampen the effect of oscillations in the solution by means of artificial diffusion. Only consistent stabilization methods have been used, which in contrast to inconsistent methods do not perturb the original transport equation. The convergence criterion for the calculations is a maximum relative error of 1×10^{-3}.

6. Experimental setup for temperature measurements in a supercritical water flow

Experimental data on supercritical water flows found in current literature has been generated in view of designing more efficient power plants. As these studies consider water at supercritical pressures as the coolant of the plant, measurements are focused on wall temperatures of the pipe with a constant wall heat flux. Local fluid temperatures are not so easy to obtain, but provide much more useful information for comparison with simulations of the temperature field.

The intention to validate the 2D simulations using temperature data of the flow therefore has led to the design and construction of an experimental setup. Accurate temperature data at different locations in the pipe has been obtained as the setup allows to measure directly into the water flow at supercritical conditions. In this section, a detailed description of the setup is followed by a comparison of test results with a 2D simulation of the lab case.

6.1. Description of the experimental setup

The main part of the setup consists of an oven containing a stainless steel pipe with an inner diameter of 10 mm that is mounted into a fluidized sand bed. The oven surrounding the fluidized bed heats the recirculating sand that keeps the pipe wall at constant temperature. The setup is schematically shown in Fig. 5, in which the thermocouples and pressure sensors are numbered for convenient referencing.

At the bottom, water is pumped into the pipe under high pressure using a HPLC pump. The water is preheated by an electric heater and trace heating cables until the desired temperature is reached at the bottom of the sand bed. This temperature is measured in the flow using a single thermocouple (TC 0) that is inserted through the bottom end of the pipe. The water is then heated further by the fluidized hot sand, which keeps the pipe wall temperature constant. Three thermocouples in row (thermocouples 1–3) measure the temperature profile in the flow. These thermocouples can be shifted in axial direction to measure at different heights. Seven additional thermocouples, coupled to the heated pipe at different heights, are used to measure the outside wall temperature of the pipe during an experiment.

Once the water has passed the oven, it is cooled to a temperature below 70 °C by a tube-in-tube heat exchanger, this is the temperature limit for the back-pressure regulator (BPR) controlling the system pressure. Air is supplied in the top section of the pipe to provide cooling for the viton sealing around the thermocouples and carries the gaseous water to the condensation section. The output signals of the thermocouples and pressure sensors are monitored and processed using LabVIEW.

6.2. Test conditions and testing procedure

Each measurement starts by shifting thermocouples 1–3 in Fig. 5 to the desired position in the pipe. After reassembling the setup, a cold test is performed to check for any leakages. Then the trace heating cables, preheater and oven are turned on to preheat the water and heat up the fluidized bed. Air cooling for the viton sealing in the top of the pipe is supplied by opening the valves to the gas cylinder filled with compressed air. An overpressure in the cylinder forces air into the pipe, where the pressure is set to 240 bar using the back-pressure regulator. The temperature controllers are tuned such that the inlet temperature measured by thermocouple 0 is maintained at 300 °C. At this point, the temperatures inside the flow measured by thermocouples 0–4 are recorded and stored in a datafile. Seven additional thermocouples, coupled to the heated pipe at different heights, are used to measure the outside wall temperature of the pipe during an experiment. The test conditions are summarized in Table 2. The procedure described above is repeated to obtain data over the effective test length of 0.45 m with steps of 5 cm.

6.3. Simulation of the supercritical water flow in the laboratory

The 2D model as described in Section 2 has been used to simulate a flow case that corresponds to the test conditions used for

Table 2
Test conditions for the temperature measurements in the lab.

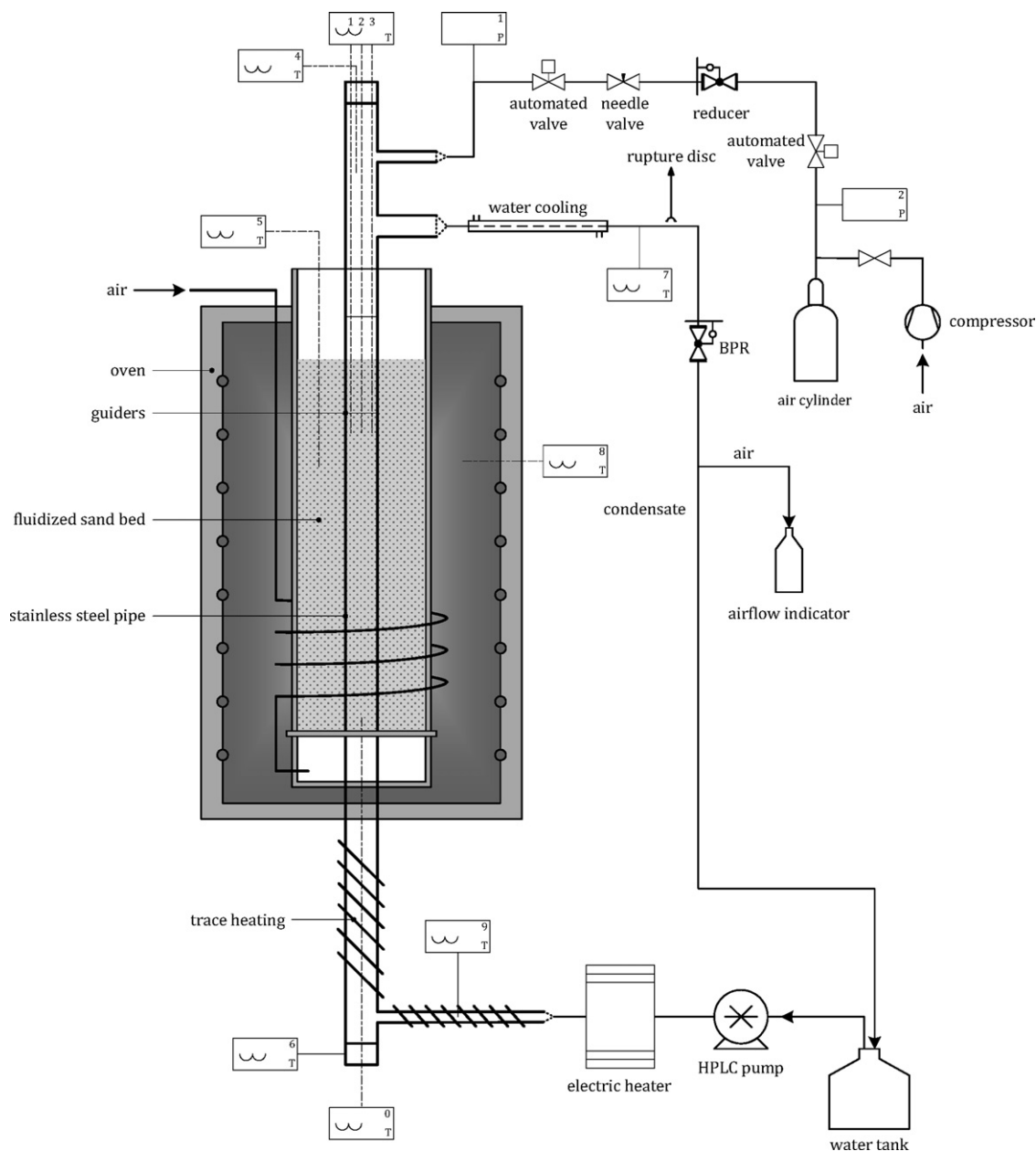| Parameter	Symbol	Unit	Value
Mass flux	G	[kg/m^2 s]	6.6, 10
Pressure	p	[bar]	240
Inner diameter	D	[mm]	10
Length of the heated pipe section	L	[mm]	450
Inlet temperature	T_{in}	[°C]	300
Wall temperature	T_w	[°C]	600

Fig. 5. Scheme of the experimental setup.

the temperature measurements in supercritical water as listed in Table 2. The mass flux was decreased in steps of 5 kg/m² s from 20 to eventually 6.6 kg/m² s, which is similar to the laboratory case. At these low mass fluxes, the 2D model predicts that the buoyancy forces are highly dominant and induce recirculation zones near the inlet. Fig. 6 shows the velocity magnitude defined in Eq. (27) and streamlines for a mass flux of 10 kg/m² s, illustrating the effect of the recirculating fluid on the flow field.

As a result of the recirculation observed in Fig. 6, the lab case simulations involve high gradients and small length scales that require a grid size of 0.05 mm. This grid is represented by the rightmost data points in Fig. 2, showing acceptable convergence for a mass flux of 6.6 kg/m² s. The pipe length has been limited to 300 mm, which covers the most interesting part of the flow and allowed the calculation to run at only one computational node. Table 3 gives an overview of the specifications for the simulated

case to generate data for validation of the 2D model in Section 6.4.

6.4. Validation of the 2D model with the experimental data

In this section, the experimental results are compared to the temperatures as calculated using the 2D model. Since the data

Table 3
Specification of the simulated cases for validation of the 2D model.

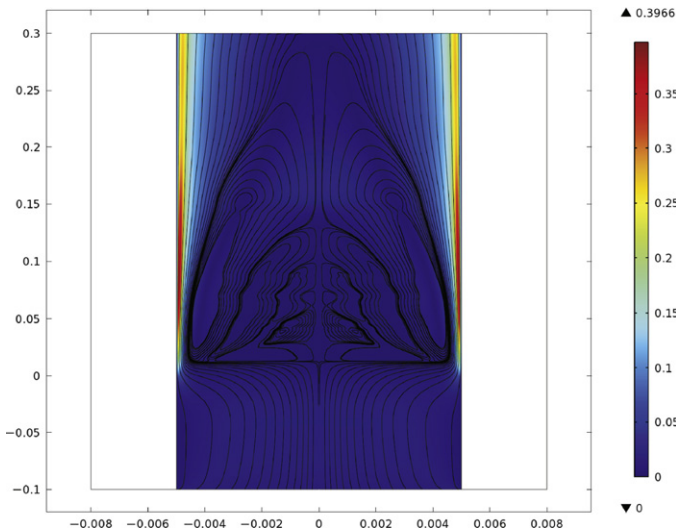| Parameter	Symbol	Unit	Value
Mass flux	G	[kg/m² s]	6.6, 10, 15, 20
Pressure	p	[bar]	240
Inner diameter	D	[mm]	10
Length of the heated pipe section	L	[mm]	300
Inlet temperature	T_{in}	[°C]	300
Wall temperature	T_{w}	[°C]	600

Fig. 6. Surface plot of the velocity magnitude with streamlines in m/s for $G = 10 \, \text{kg/m}^2 \, \text{s}$. The coordinates on the axes are expressed in meters.
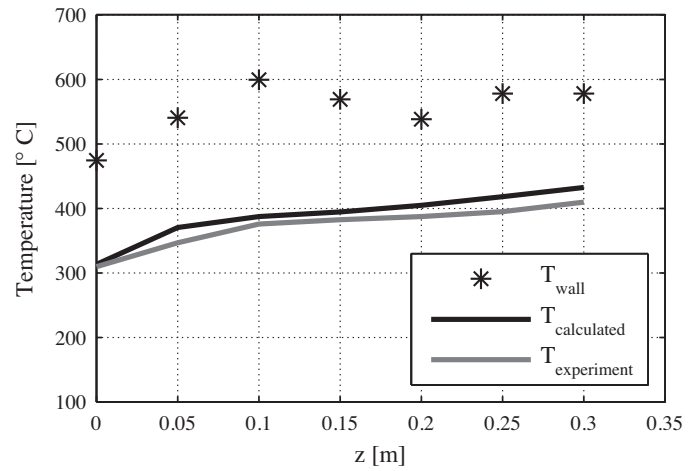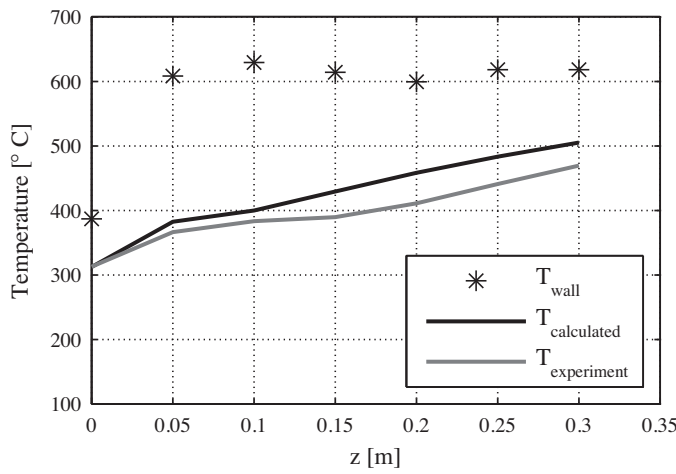

Fig. 7. Comparison of the 2D lab case simulation with the experimental data ($G = 6.6 \, \text{g/m}^2 \, \text{s}$).

points obtained with thermocouples 1–3 are to be compared with results of steady state calculations, they have been time-averaged using:

$$\overline{T} = \frac{1}{3} \sum_{i=1}^{3} \left[\frac{1}{n+1} \sum_{j=0}^{n} T_i(t_0 + n\Delta t) \right] \tag{24}$$

where i denotes the thermocouple index, ΔT is 1 s and n are the number of seconds taken from the data set. The time-averaged temperatures measured inside the flow are plotted with the surface-averaged numerical solutions for a mass flux of $G = 6.6 \, \text{kg/m}^2 \, \text{s}$ in Fig. 7 and a mass flux of $G = 10 \, \text{kg/m}^2 \, \text{s}$ in Fig. 8. Both figures show that the 2D model slightly over predict the

Fig. 8. Comparison of the 2D lab case simulation with the experimental data ($G = 10 \, \text{kg/m}^2 \, \text{s}$).

Table 4
Boundary conditions for the 2D heat transfer model.

Boundary	Condition	Symbol	Unit	Value
Inlet	Mass flux	G	[kg/m^2 s]	200
Inlet	Temperature	T_{in}	[°C]	350
Heated wall ($z > 0$)	Temperature	T_w	[°C]	600
Outlet	Relative pressure	p_{out}	[bar]	0

temperature measured in the setup. It is assumed that the small deviations are mainly caused by the effect of the recirculation zone present in the flow. The recirculation provides mixing of the fluid, thereby enhancing the heat transfer.

The good agreement between the numerical and experimental data as seen above proves that the 2D model is accurate for low mass fluxes. When the flow fields shown in Fig. 6 for $G = 10 \, \text{kg/m}^2 \, \text{s}$ and Fig. 16 for $G = 200 \, \text{kg/m}^2 \, \text{s}$ are compared, it is clear that buoyancy forces are far less dominant over the pressure forces in the latter case. For this reason, possible errors due to the recirculation of the fluid will not occur at higher mass fluxes. The accuracy of the 2D model for these cases is expected to be accurate because the flow is easier to calculate due too smaller buoyancy effects.

7. Boundary conditions

The boundary conditions used for the 2D calculations are indicated in the computational domain in Fig. 9. The fluid enters the pipe with a uniform velocity profile, passes an insulated entrance section of 0.1 m and is then heated over a length of 2.5 m using a constant wall temperature. At the outlet, it is assumed that the relative pressure, the normal shear stresses and the normal heat flux are zero. In order to allow for fluid data import into COMSOL, all fluid properties in the 2D calculations are evaluated at a fixed reference pressure of 300 bar. This simplification introduces only a small
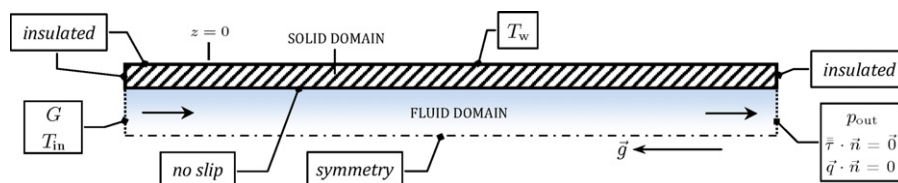

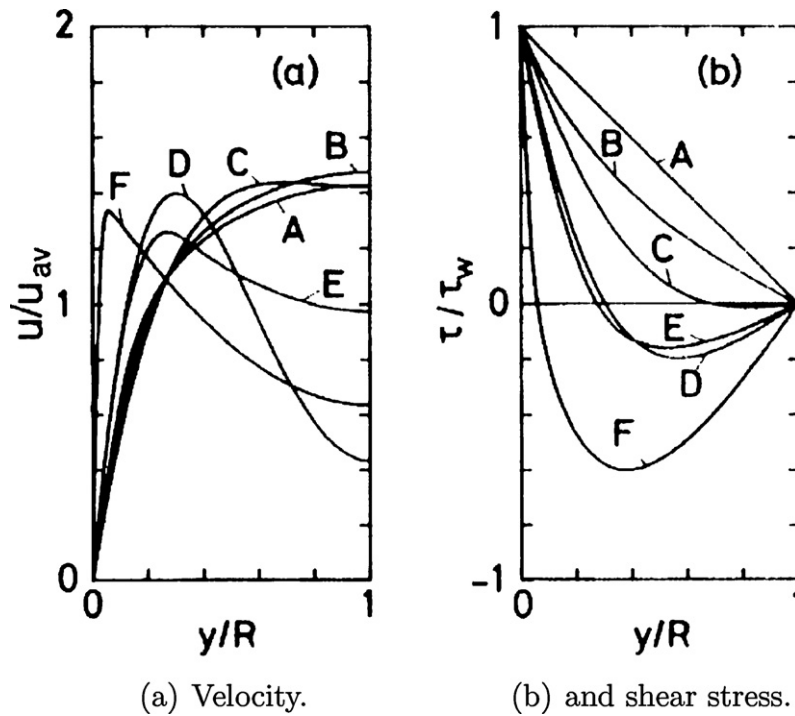**Fig. 9.** Boundary conditions for the 2D heat transfer model, indicated in the computational domain.

Fig. 10. Distributions at various Grashof numbers at a constant $Re = 3000$. A, $Gr = 2.1 \times 10^3$, turbulent; B, $Gr = 6.1 \times 10^4$, turbulent; C, $Gr = 8.8 \times 10^4$, laminar; D, $Gr = 2.7 \times 10^5$, laminar; E, $Gr = 3.3 \times 10^5$, turbulent; F, $Gr = 9.2 \times 10^6$, turbulent [10].

error since the pressure inside the pipe is more or less constant and the fluid properties are weak functions of the pressure. The specifications for the mass flux, the pressure and the temperatures shown in Fig. 9 are listed in Table 4.

The ends of the solid domain and the outer wall of the entrance section are assumed to be perfectly insulated. A no-slip condition is applied to the velocity at the inner wall. The corresponding wall conditions for k and ϵ in the low-Reynolds formulation are:

$$k = 0 \tag{25}$$

$$\epsilon = 2\frac{\mu}{\rho}\frac{k}{l_w^2} \tag{26}$$

(a) Normal heat transfer.

(b) Enhancement.

(c) Impairment of enhanced heat transfer.

(d) Deterioration.

(e) Recovery.
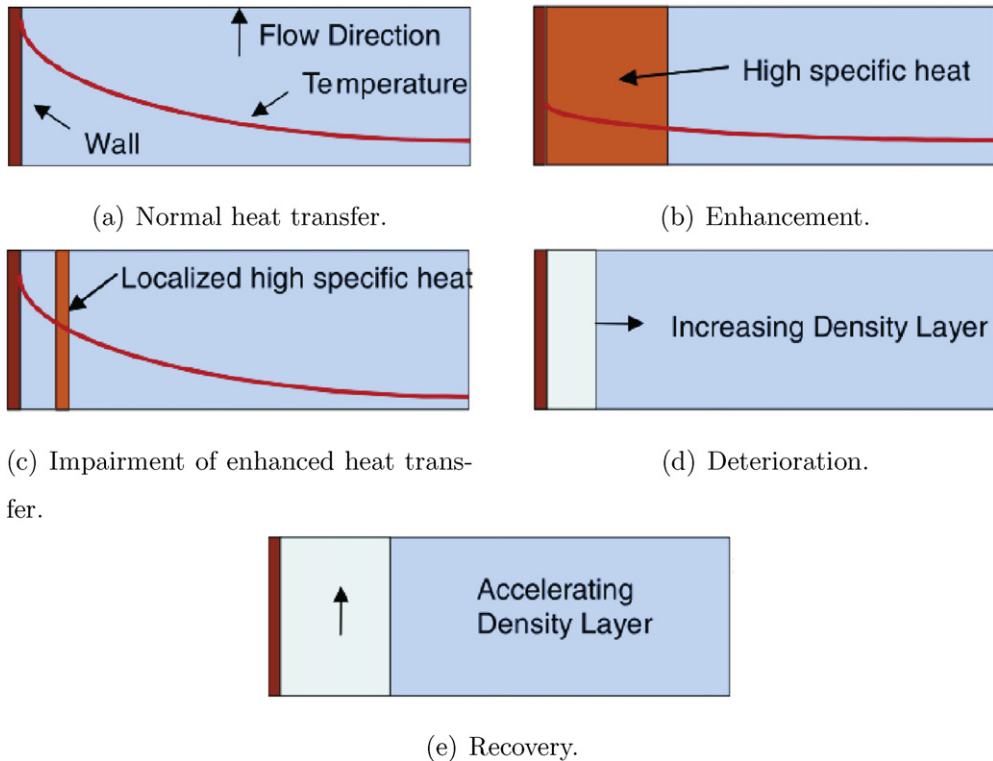
Fig. 11. Illustration of the different heat transfer regimes [11].

where l_w is the distance to the closest wall, calculated using Eq. (21). The symmetry condition at the centerline in Fig. 9 prescribes zero flux and vanishing shear stresses.

8. 2D simulation results

This section presents the results of the heat transfer simulations in the 2D computational domain as shown in Section 2 for the case specified in Section 7. The results shown below give detailed information on the flow field and heat transfer over the cross-section of the pipe. The solution gives insight into the effect of the phase transition on the heated water flow, and analysis of the variations in radial direction allows to assess the 'plug flow' assumption in the 1D model. Figs. 10 and 11 are used to give better insight in the velocity profiles stress distributions and types of heat transfer which are typically found in heat transfer to supercritical fluids. A quantitative comparison with the 1D results presented in Sallevelt et al. [4] can be found in Section 9.

Fig. 12 shows a surface plot of the isobaric heat capacity, where the solution is projected onto the surface of the computational domain. The domain has been mirrored in the centerline of the pipe to obtain a view on the full cross-section and the geometry has been scaled for convenient visualization. Since the isobaric heat capacity reaches a maximum at the pseudo-critical point, the plot indicates where the phase transition to supercritical water takes place. It can be seen that the pseudo-critical point is reached in a thin layer that sticks close to the wall over a long distance, separating gaseous supercritical water adjacent to the wall from the liquid bulk flow at sub-critical temperatures. This pseudo-critical region slowly moves toward the center until the bulk flow reaches the pseudo-critical temperature around 1.5 m pipe height. The bulk flow has still not completely passed the phase trajectory after the total heated length of 2.5 m, which means the mean outlet temperature will be far from the desired 600 °C.

The plot in Fig. 13 represents the temperature field with isotherms. The flow is heated from 350 °C at the inlet to a mean temperature of 424 °C at the outlet by the hot wall of 600 °C. From the mutual distance between the isotherms it can be concluded that the temperature increase is fastest near the inlet and is slowest where the bulk flow reaches the pseudo-critical temperature. The pseudo-critical region acts like a heat sink due to the high heat capacity, which causes the temperature to rise more slowly.
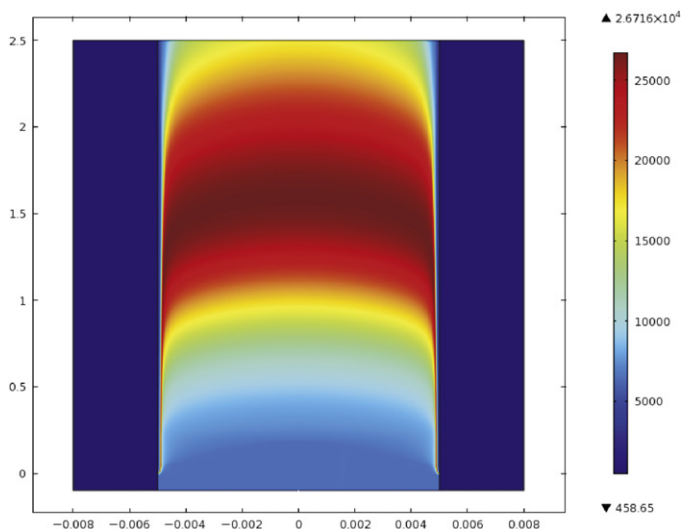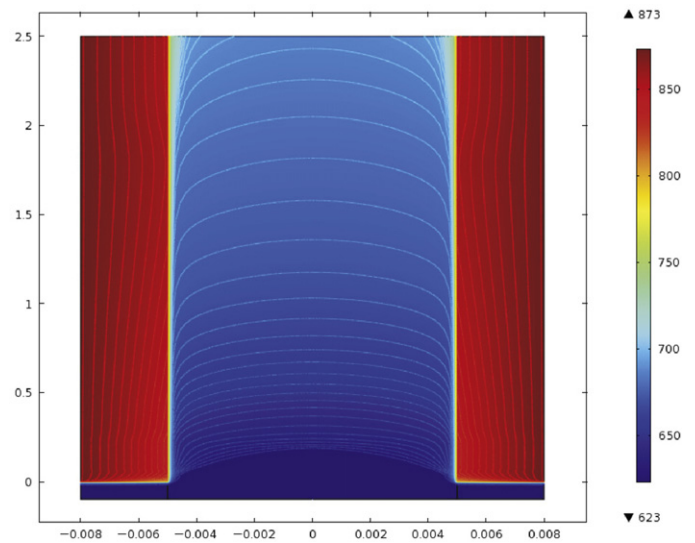

Fig. 13. Surface plot of the temperature in K. The coordinates on the axes are expressed in meters.

Furthermore, less heat is transported from the wall through the supercritical region due to the steep decrease in conductivity [4].

Fig. 14 shows the temperature profiles at different pipe heights. The figure gives better insight into the temperature gradient near the wall and the influence of the phase transition on the temperature variations over the radius. In general, the profiles over the diameter are sufficiently uniform to justify the plug flow assumption that was made for deriving the 1D model equations.

The velocity plot in Fig. 15 shows the velocity magnitude, which is defined as:

$$U = \sqrt{u_r^2 + u_z^2} \tag{27}$$

where u_r and u_z are the velocities in radial and longitudinal direction. It can be noted that the no slip condition at the wall is satisfied. The fluid is accelerated in the pseudo-critical regions due to buoyancy forces and volumetric expansion. The increased velocity near the wall in the lower half of the pipe causes suction of fluid from
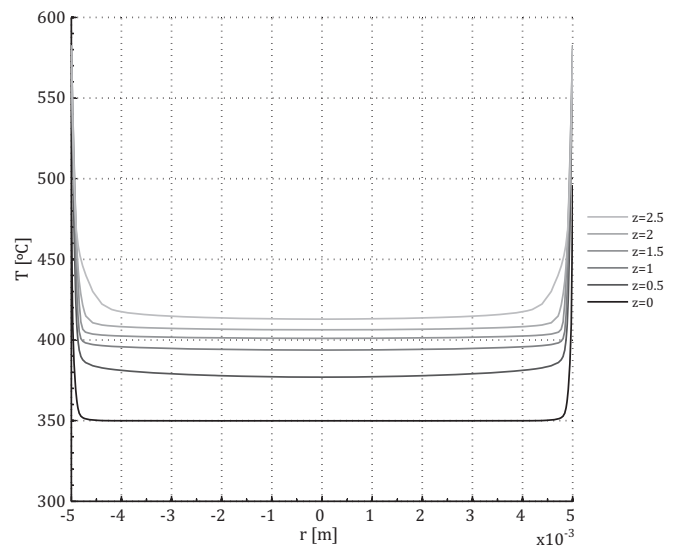

Fig. 12. Surface plot of the isobaric heat capacity in J/kg K. The coordinates on the axes are expressed in meters.

Fig. 14. Temperature profiles taken at different pipe heights. The temperatures are expressed in °C and the pipe heights are given in meters.
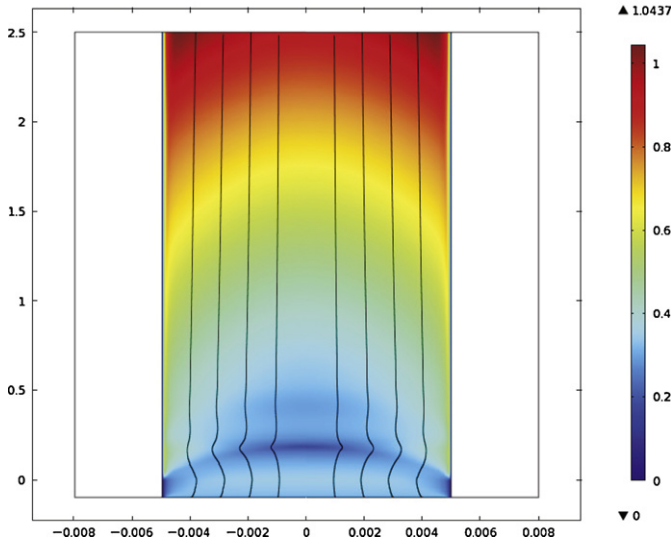
Fig. 15. Surface plot of the velocity in m/s. The coordinates on the axes are expressed in meters.

Fig. 17. Surface plot of the density in kg/m³. The coordinates on the axes are expressed in meters.

the bulk flow toward the wall, which results in the hump in the streamlines shown in the figure.

The velocity magnitude over the radius at different pipe heights is plotted in Fig. 16. The profiles show that the flow along hot pipe wall does not resemble a plug flow. This finding contradicts the conclusion of the temperature profile analysis above. The plug flow assumption on which the 1D model is based may be considered inaccurate when it comes to the flow field, but the 1D model cannot be disqualified on beforehand as the temperature field is probably more important for heat transfer simulations. A comparison with typical velocity profiles as given in the work of Sallevelt et al. [4] shows that the flow is turbulent, with high Grashof numbers at the start of the heated pipe section. The velocity profile at $z = 0$ in Fig. 16 is not yet influenced by heating effects and therefore resembles profile A for low Grashof numbers in Fig. 11(a). As soon as the fluid enters the heated section of the pipe, the velocity profile is quickly transformed to profile F due to strong buoyancy forces. The velocity
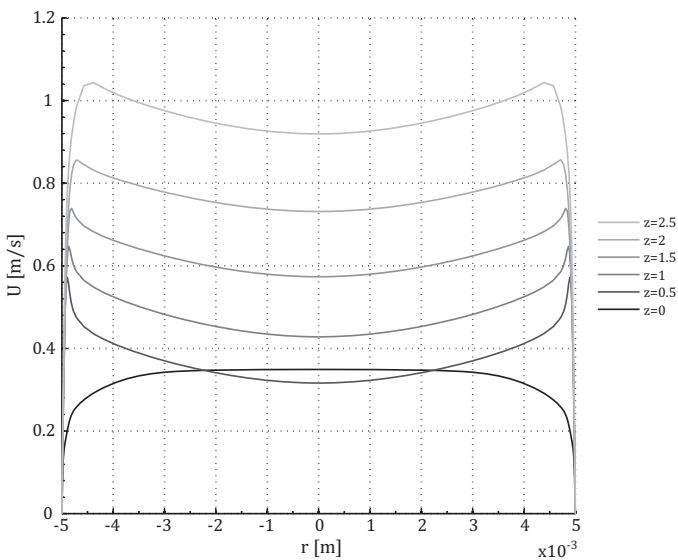
differences over the radius then decrease toward the outlet because of the accelerating bulk flow. At the outlet, the velocity profile is similar to profile E.

The thin pseudo-critical region near the wall that is observed in Fig. 12 leads to very large density differences over the pipe diameter. This can be clearly seen in the density plot in Fig. 17. The high gradient in density suggests that the critical heat flux has been exceeded and pseudo-film boiling is taking place at the wall. In the work of Sallevelt et al. [4] it is pointed out that film boiling causes deterioration of the heat transfer and should therefore be avoided if possible.

In order to verify the presumption that pseudo-film boiling occurs near the pipe wall, the solution has been recalculated with a wall temperature that linearly increases from inlet temperature (350 °C) at $z = 0$ to the original wall temperature (600 °C) at $z = 2.5$ m to capture the onset of this effect. The wall heat flux at the location where the onset of film boiling is observed can then be compared with the predictions for the critical heat flux as predicted by Mokry et al. [12,4]. The simulation using a gradually increasing wall temperature resulted in the density plot shown in Fig. 18. It can be seen

Fig. 16. Velocity profiles taken at different pipe heights, with a mass flux of 200 kg/m² s. The pipe heights are given in meters.

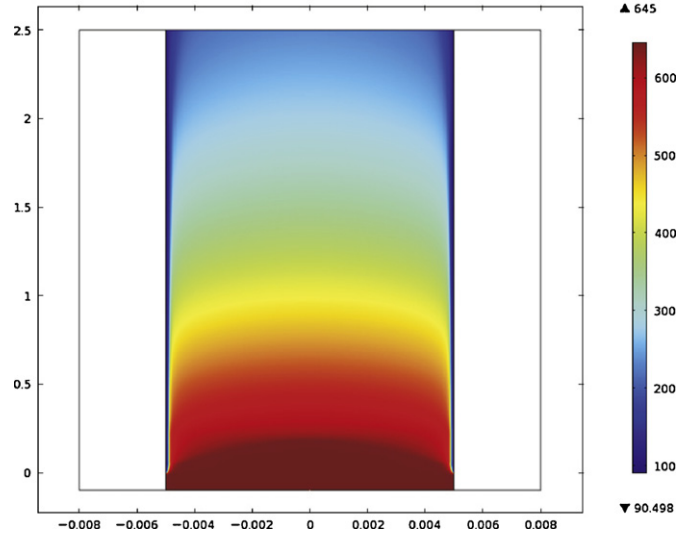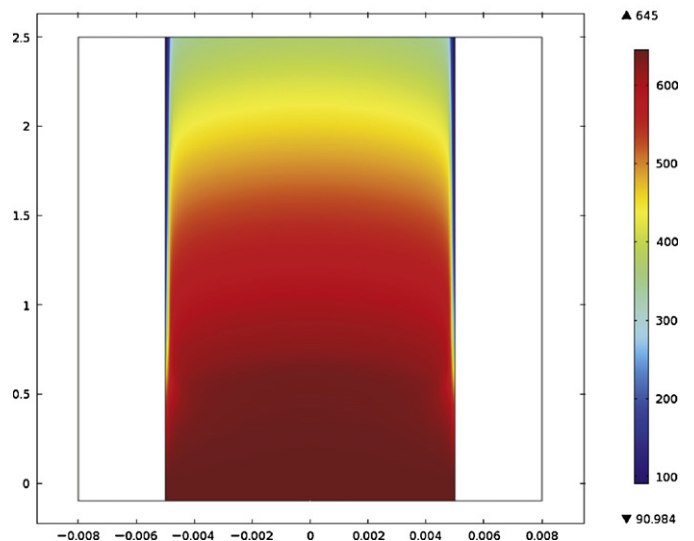**Fig. 18.** Surface plot of the density in kg/m³ for the case with linearly increasing wall temperature. The coordinates on the axes are expressed in meters.
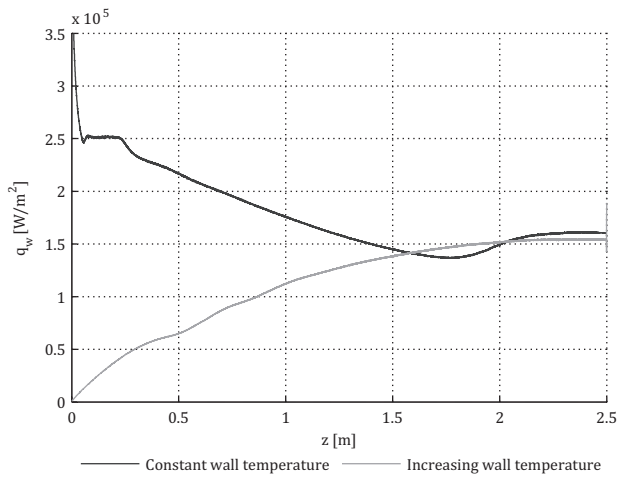
Fig. 19. Wall heat flux as function of the pipe height using a constant wall temperature and a linearly increasing wall temperature.
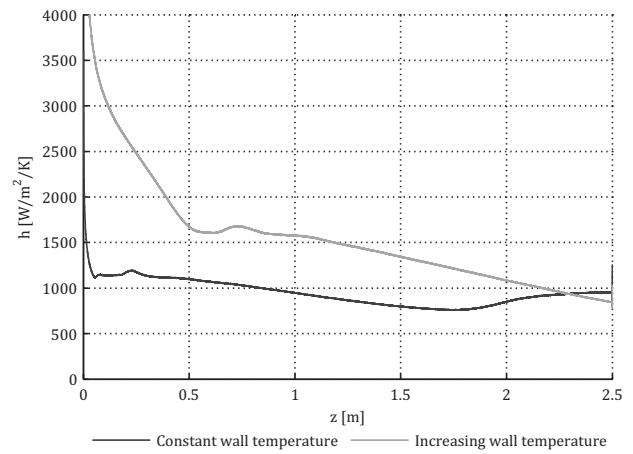

Fig. 20. Heat transfer coefficient as function of the pipe height using a constant wall temperature and a linearly increasing wall temperature.

that the onset of pseudo-film boiling is located at approximately $z = 0.75$ m.

Fig. 19 shows the wall heat flux as function of the pipe height for both the constant and the linearly increasing wall temperature cases. The line corresponding to the simulation with increasing wall temperature indicates that the wall heat flux at $z = 0.75$ m is about 90 kW/m^2. This value is very close to the critical heat flux for $G = 200$ kg/m^2 s as predicted by the correlations of Yamagata et al. [13] and Mokry et al. [14]. The good agreement of the critical heat flux as obtained from the 2D simulations with the empirical correlations from literature is a confirmation of the occurrence of pseudo-film boiling.

The heat transfer efficiency for both cases can be assessed by comparing the heat transfer coefficients given in Fig. 20. The heat transfer coefficient has been calculated using the wall heat flux, wall temperature and temperature at the centerline according the following equation:

$$h = \frac{q_w}{T_w - T_{ax}} \tag{28}$$

The shape of the line for constant wall temperature can be recognized in the line for the gradually increasing wall temperature,

but is shifted upwards in the pipe because of the later onset of film boiling. By comparing the graphs in Figs. 19 and 20 it can be concluded that a higher temperature difference generally leads to an increase in heat flux, but at the same time to a less efficient heat transfer regime.

In order to gain more insight into the behavior of the heat transfer coefficient over the pipe length, all parameters involved in Eq. (28) are plotted in one figure for each of the heating methods. Fig. 21 shows how the heat transfer coefficient, wall temperature, centerline temperature and wall heat flux are related for the case of constant wall temperature. The values of the first three parameters in the list can be read from the left axis, while the wall heat flux is indicated by the right axis.

The small increase of the heat transfer coefficient around $z = 0.2$ m coincides with the location where the centerline temperature starts to rise. Since the heat flux and wall temperature are constant, the result is a smaller temperature difference and thus a higher heat transfer coefficient. This effect is however quickly followed by a decline in heat transfer due to a growing low-density layer near the wall (Fig. 11(d)). While both the wall temperature and centerline temperature increase very slowly, deterioration of the heat transfer continues until the bulk flow has passed the
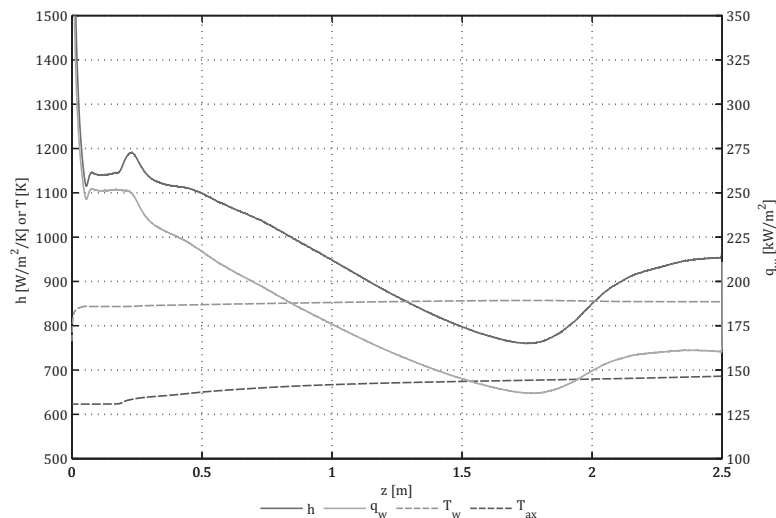

Fig. 21. Heat transfer coefficient, wall heat flux, wall temperature and centerline temperature as function of the pipe height for the case with a constant wall temperature.
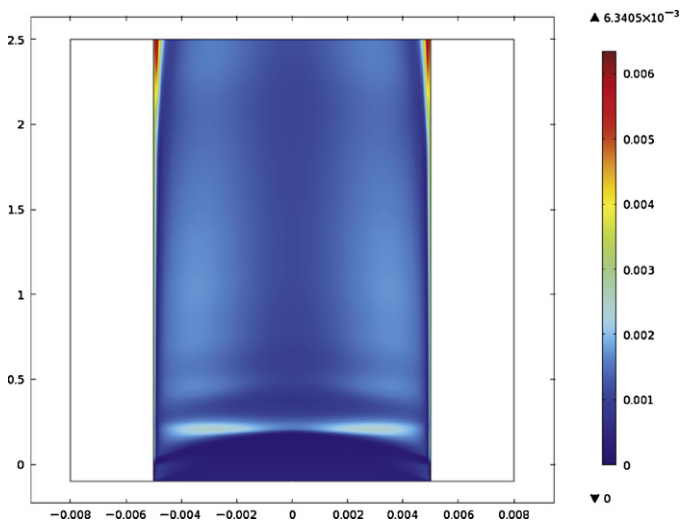
Fig. 22. Surface plot of the turbulent kinetic energy in m^2/s^2 for the case with constant wall temperature. The coordinates on the axes are expressed in meters.
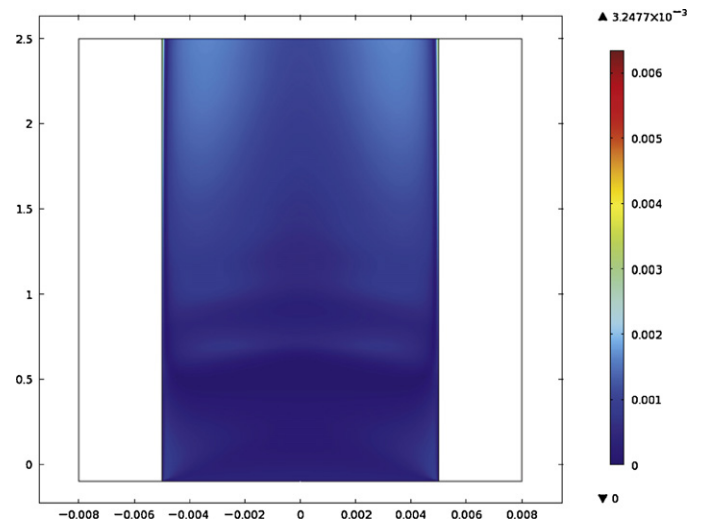

Fig. 24. Surface plot of the turbulent kinetic energy in m^2/s^2 for the case with increasing wall temperature. The coordinates on the axes are expressed in meters.

pseudocritical point. From this point, the heat flux is recovering (Fig. 11(e)) and the wall temperature starts to decrease slowly.

The severe impairment of heat transfer at high heat flux and the recovery further downstream where the bulk temperature passes the pseudo-critical temperature have been noted in Jackson and Hall [15] on the basis of experimental data. The authors suggest that deterioration of heat transfer may be related to the turbulence near the boundary layer. This explanation has been adopted in other literature [4] and may also explain the recovery of heat transfer observed in Fig. 21. The turbulent kinetic energy plot in Fig. 22 shows high turbulence production in that particular region, which may well be responsible for the increase in heat flux.

Fig. 23 shows the parameter values that characterize the heat transfer for the case of gradually increasing wall temperature. The brief increase of the heat transfer coefficient at $z = 0.6$ m occurs at the location where the temperature in the boundary layer equals the pseudo-critical temperature. The local phase change at the wall results in a larger slope of the heat flux over a few centimeters, but then the slope restores due to the gaseous layer that is formed at the wall. From this point, around $z = 0.75$ m, the critical heat flux is reached and heat transfer starts to deteriorate. The heat transfer

coefficient does not show the recovery that is observed in Fig. 21. In the plot of the turbulent kinetic energy in Fig. 24, where the color scale is identical to the scale in Fig. 22, it can be seen that there is hardly any turbulence production near the wall. This is in agreement with the assumption that the turbulent diffusivity is causing the recovery in heat transfer for the case of constant wall temperature.

9. Comparison of 1D and 2D simulation results

The results of the 1D model have been compared with averaged quantities over the cross-section as obtained with the 2D model, for the case as presented in Table 4 and a numerical grid of 700,717 elements. First, the results are compared when the heat transfer coefficient data from the 2D simulation is directly used for the 1D calculations. This way, deviations due to mismatching heat transfer predictions by a Nusselt correlation from literature are excluded. The comparison will hence give a good indication for the loss of accuracy when neglecting 2D effects in the model equations. Subsequently, the 1D results on basis of the Nusselt correlations from
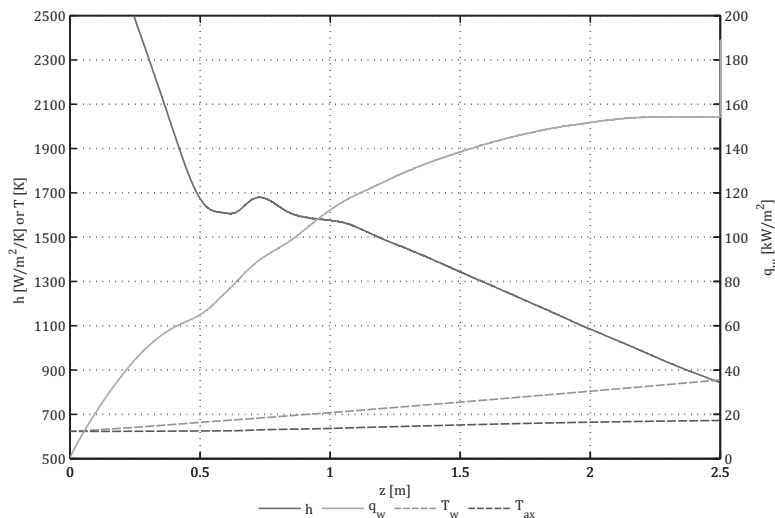

Fig. 23. Heat transfer coefficient, wall heat flux, wall temperature and centerline temperature as function of the pipe height for the case with increasing wall temperature.
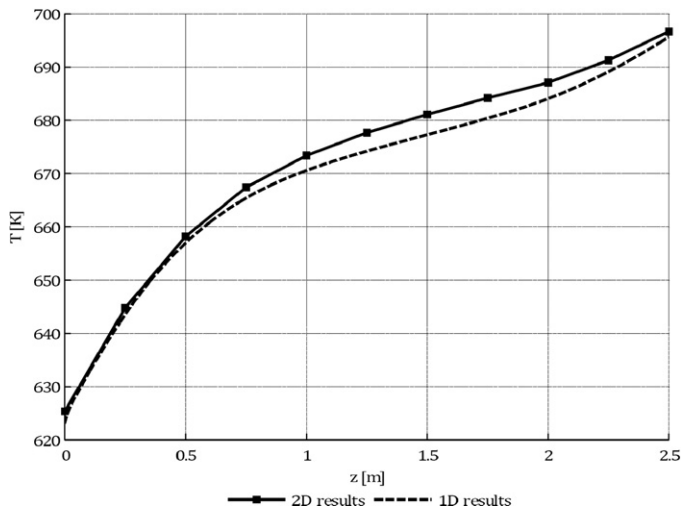
Fig. 25. Temperature as function of the pipe height for $G = 200 \, \text{kg/m}^2$ s. The 2D results are averaged over the cross-section and the 1D results are calculated on basis of heat transfer data from the 2D simulations.

Fig. 27. Parameter of Aicher and Martin [16] as function of the pipe height for $G = 200 \, \text{kg/m}^2$ s. The parameter is calculated using the 1D model on basis of heat transfer data from the 2D simulations.

literature are compared to assess which of them is most suitable for the case that is studied.

Fig. 25 shows the temperature results for both models in case the Nusselt correlation in the 1D model is replaced by heat transfer coefficient data from the 2D solution. Here the heat transfer coefficient as function of the pipe height has been calculated according to Eq. (28). In fact, the Nusselt correlation is now ideal for the simulated case. The deviations between the lines seen in Fig. 25 are therefore mainly caused by the simplifications applied to the governing equations to arrive at the 1D model equations described in the work of Sallevelt et al. [4]. With a maximum temperature difference of about 5 K, the loss of accuracy is quite limited.

The velocity plot in Fig. 26 shows a very reasonable correspondence between the two models as well. However, the 1D calculations seem to be unsuitable for very long pipes because the deviation increases with the pipe height.

The coupling of the 1D model equations with heat transfer data from the 2D results gives the opportunity to investigate the influence of buoyancy forces on the flow according to the 2D simulations. The contribution of free convection to the heat transfer is characterized by the parameter of Aicher and Martin [16]. The value
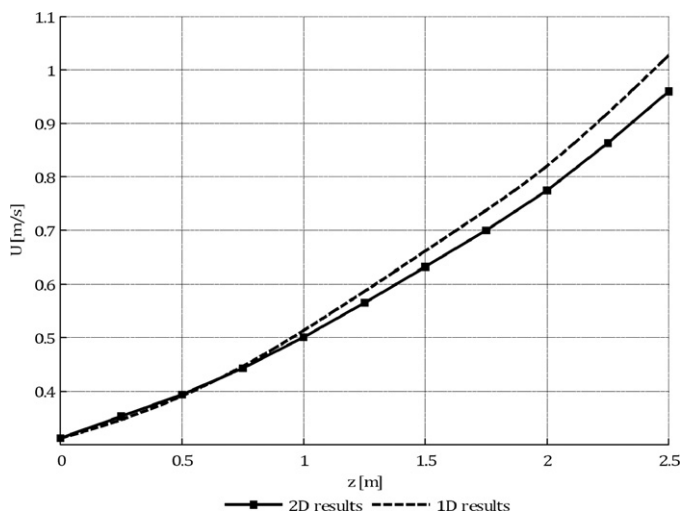
of this parameter as function of the pipe height is shown in Fig. 27. When the values are compared with Fig. 30(a) for aiding flow, it can be seen that the flow is mainly driven by free convection. The decrease of the parameter value toward the outlet is caused by acceleration of the bulk flow. These observations are in accordance with the velocity profiles shown in Fig. 16.

The same analysis has also been performed for a mass flux of $1000 \, \text{kg/m}^2$ s to verify the relation between the velocity profiles and the buoyancy forces according to the parameter of Aicher and Martin [16]. In Fig. 28, it can be seen that the velocity profiles for this mass flux are far less deformed by buoyancy effects than is the case in Fig. 16 for $G = 200 \, \text{kg/m}^2$ s.

On the basis of the velocity profiles shown in Fig. 28, it is expected that the heat transfer is mainly driven by forced convection. This flow classification has been confirmed by the parameter of Aicher and Martin [16] after loading the heat transfer coefficient as calculated by the 2D model into the 1D model. Fig. 29 shows that

Fig. 26. Velocity as function of the pipe height for $G = 200 \, \text{kg/m}^2$ s. The 2D results are averaged over the cross-section and the 1D results are calculated on basis of heat transfer data from the 2D simulations.
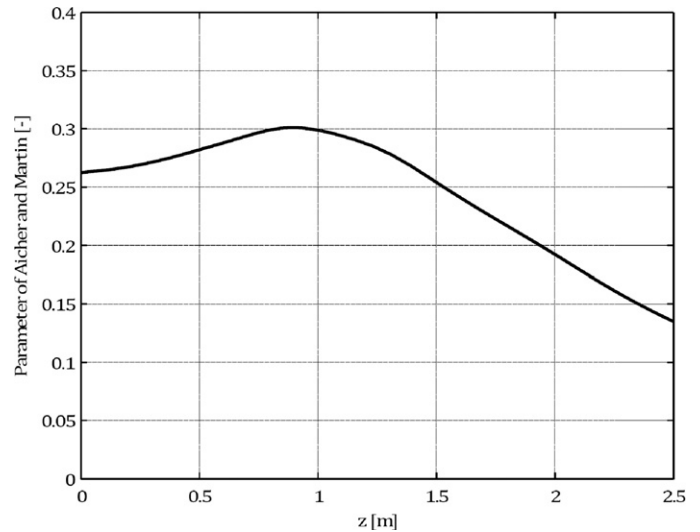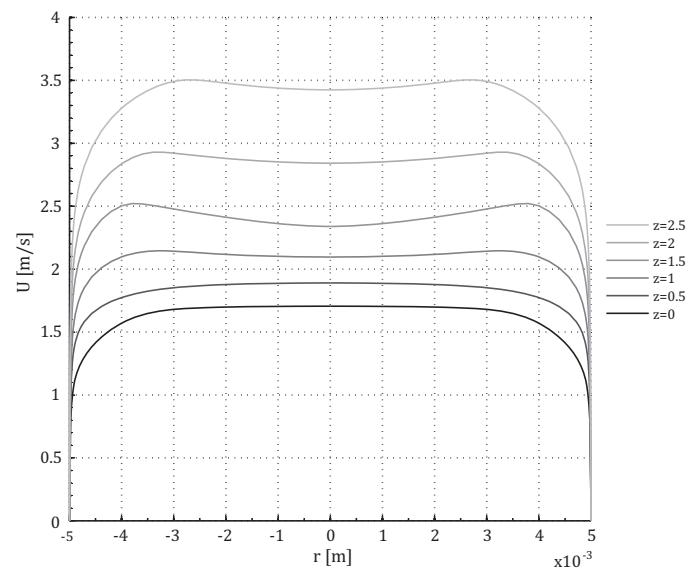

Fig. 28. Velocity profiles taken at different pipe heights for the case with a mass flux of $1000 \, \text{kg/m}^2$ s.

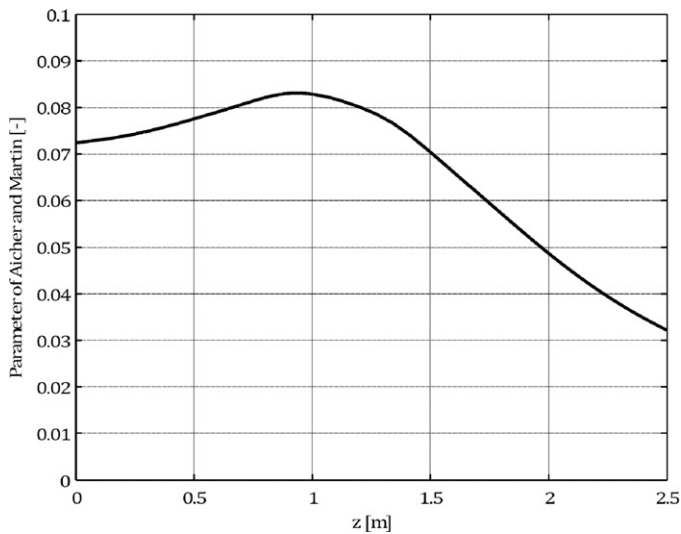**Fig. 29.** Parameter of Aicher and Martin [16] as function of the pipe height for $G = 1000$ kg/m^2 s. The parameter is calculated using the 1D model on the basis of heat transfer data from the 2D simulations.

Fig. 31. Temperature as function of the pipe height for $G = 200$ kg/m^2 s. The 2D results are averaged over the cross-section and the 1D results are calculated on basis of different Nusselt correlations from literature.

Fig. 32. Isobaric heat capacity as function of the pipe height for $G = 200$ kg/m^2 s. The 2D results are averaged over the cross-section and the 1D results are calculated on the basis of different Nusselt correlations from literature.

the parameter values are below 0.1, which indicates that forced convection is the dominant heat transfer mechanism according to Fig. 30(a).

When the Nusselt correlations from literature are used, the results for the two models are given in Fig. 31. The plot shows that the correlations that were derived for other pipe diameters than 10 mm [17,16] lead to temperatures that do not correspond with the 2D results. The temperature of the fluid is much better described if the correlation of Mokry et al. [14] or Swenson et al. [18] is used, which were derived for pipes with similar geometry as used in the simulations. Although the correlation of Yamagata et al. [13] was also obtained from measurements on a 10 mm pipe, the agreement is much worse. This may be explained by the fact that the measurements showing heat transfer deterioration were excluded from the dataset used to derive the correlation. The line for the Mokry et al. [14] correlation shows a very close match until the bulk flow passes the pseudo-critical point after 1.5 m. The length required for the phase transition of the bulk according to the 1D model is shorter, which implies that the heat transfer as predicted by the Nusselt correlation is higher.

The lines indicating the isobaric heat capacity in Fig. 32 confirm that the predicted heat transfer coefficient by the correlation of
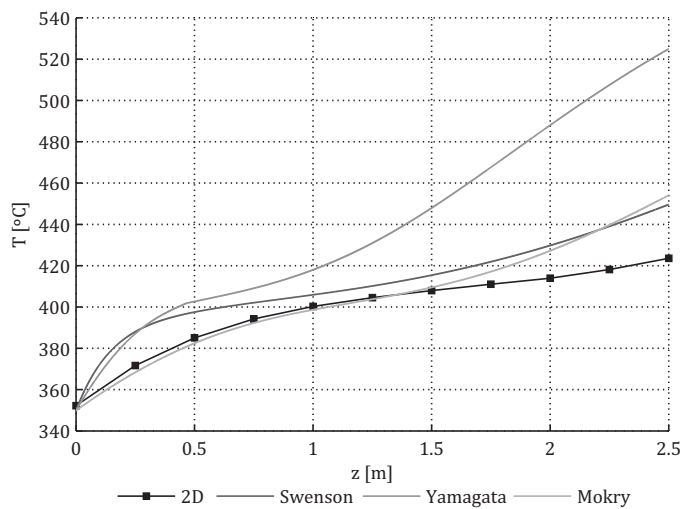

(a) Aiding flow.

(b) Opposing flow.

Fig. 30. Schematic view of the influence of buoyancy forces on heat transfer [16].

Fig. 33. Velocity as function of the pipe height for $G = 200$ kg/m² s. The 2D results are averaged over the cross-section and the 1D results are calculated on basis of different Nusselt correlations from literature.
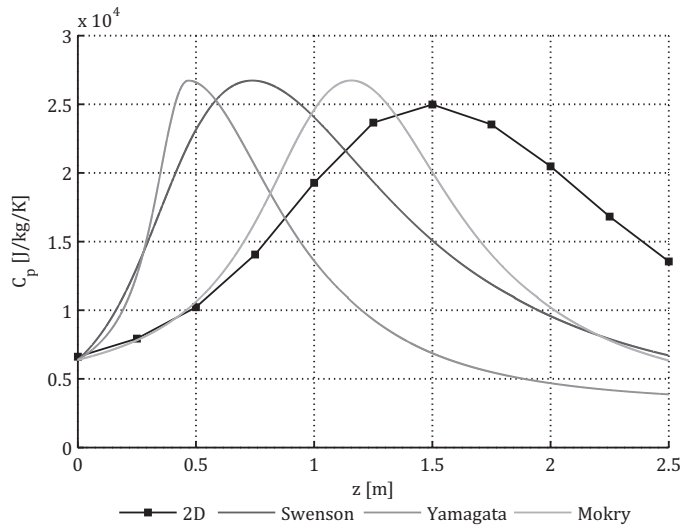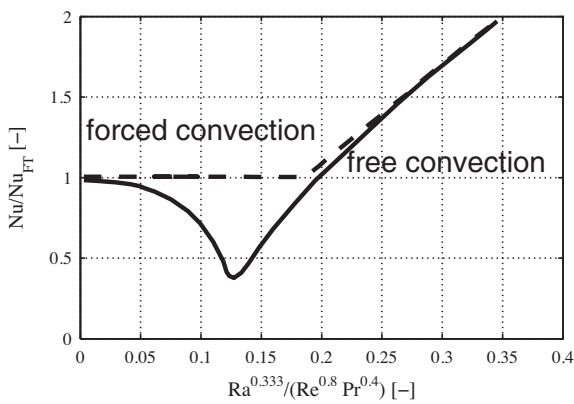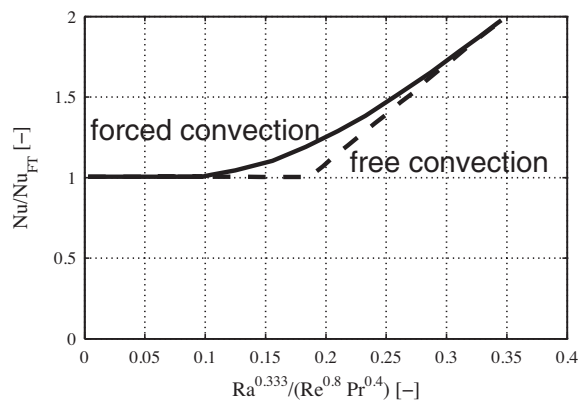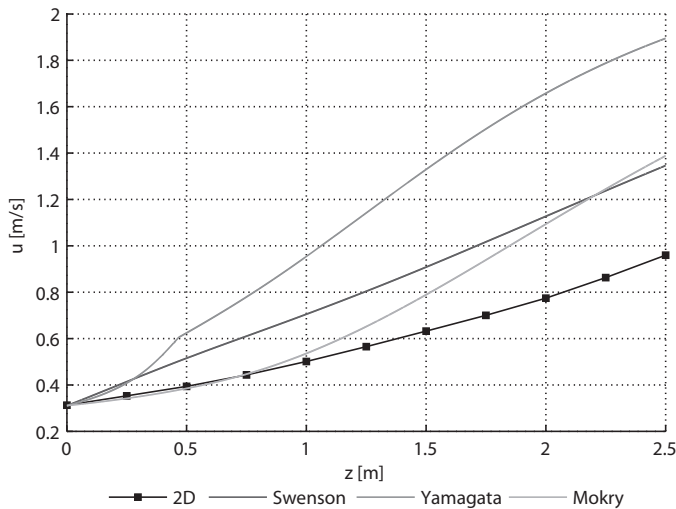
Mokry et al. [14] is closest to the results of the 2D model. The shape of the curve is however best predicted by Swenson et al. [18].

The location of the phase transition is represented by an increase of the fluid velocity shown in Fig. 33. All correlations predict the phase transition in the bulk to occur earlier in the pipe and faster. As a consequence, the acceleration of the flow starts earlier and the slope of the lines is higher. Over the second half of the pipe, none of the lines resulting from the 1D calculations matches the 2D results satisfactorily.

From the figures presented in this section, it follows that the correlation of Mokry et al. [14] gives the best results for the first section of the pipe and then Swenson et al. [18] gives better predictions for the remaining pipe length. In Fig. 34 it can be seen that the heat flux of the 2D model would indeed be best approximated by using a combination of those two Nusselt correlations. However, the incapability of the individual correlations to predict the heat transfer coefficient accurately over the entire pipe length makes the 1D model unsuitable as a modeling tool for applications using the unique properties of supercritical water.
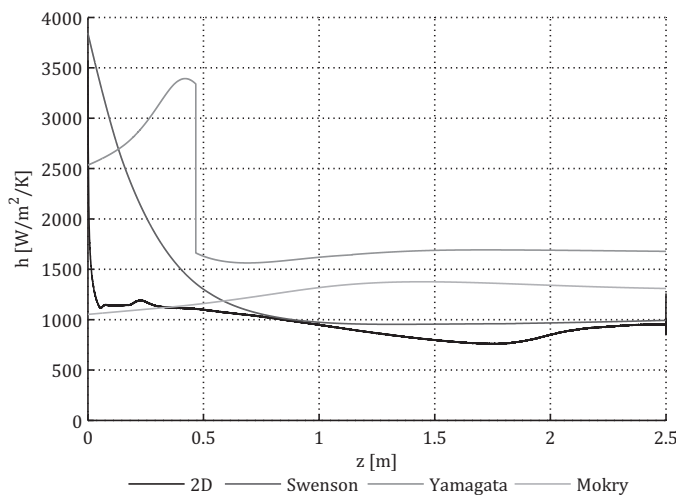

Fig. 34. Heat transfer coefficient as function of the pipe height for $G = 200$ kg/m² s. The 2D results are averaged over the cross-section and the 1D results are calculated on the basis of different Nusselt correlations from literature.

10. Conclusions

The simulations in a two-dimensional domain have been performed using the low-Reynolds k–ϵ model and the IAPWS-IF97 formulation. Using the simulation results it is clearly visible at which position the phase transition to supercritical water takes place in the geometry, since the isobaric heat capacity reaches a maximum at the pseudo-critical point. An interesting feature of the phase transition is that the pseudo-critical point is reached in a thin layer that sticks close to the wall over a long distance, separating gaseous supercritical water adjacent to the wall from the liquid bulk flow at sub-critical temperatures. The pseudo-critical region acts like a heat sink due to the high heat capacity, which causes the temperature to rise slowly. Furthermore, less heat is transported from the wall through the supercritical region to the bulk flow due to the steep decrease in conductivity in the proximity of the critical point [4]. The fluid is accelerated in the pseudo-critical regions due to buoyancy forces and volumetric expansion. The increased velocity near the wall in the lower half of the pipe causes suction of fluid from the bulk flow toward the wall. This results in non-uniform velocity profiles over the radius.

A comparison of the critical heat flux from the 2D simulations with empirical correlations from literature show that pseudo-film boiling occurs for the $G = 200$ kg/m² s case. Pseudo-film boiling could be a cause of deterioration of the heat transfer, and should therefore be avoided if possible. The good agreement of the critical heat flux as obtained from the 2D simulations with the empirical correlations from literature is a confirmation that the 2D model is able to predict the occurrence of pseudo-film boiling.

The occurrence of pseudo-film boiling results in the effect that a higher temperature difference between the wall and the bulk temperature leads to an increase in heat flux, but at the same time leads to a less efficient heat transfer regime. The results of the heat transfer calculations for the chosen flow conditions point out that pseudo-film boiling occur when the critical heat flux is exceeded. The critical heat flux for the onset of this effect is well described by the correlations of Yamagata et al. [13] and Mokry et al. [14]. Heat transfer deterioration is observed over a large part of the heated pipe section, which can be associated with the localized peak in heat capacity and growing low-density layer. Pseudo-film boiling can be suppressed by increasing the turbulence near the boundary layer or by limiting the temperature difference between the wall and the fluid. The heat transfer partly recovers once the bulk flow has passed the pseudo-critical point. According to the numerical results, the recovery is caused by increased turbulence production near the wall. These findings are in agreement with the phenomena described in literature.

The 2D model results have been compared with results from a 1D model using several Nusselt correlations from literature. It is clear that that the results do not correspond well when a Nusselt correlation is used which is derived for a pipe flow in a different pipe diameter. Nusselt correlations derived for a pipe flow with the same pipe diameter show a better comparison. However, each individual Nusselt correlation from literature shows an incapability to predict the heat transfer coefficient accurately over the entire pipe length. Therefore it can be concluded that 1D models should not be used to simulate the heat transfer to supercritical water in long or complex pipe configurations.

Fluid temperatures of a supercritical water flow have been successfully measured using a new setup. The experiments for validation of the 2D model have been conducted for a low mass flux and a shorter pipe than originally planned because of practical limitations. At these conditions, the 2D model predicts recirculation zones near the inlet which result in a more complex simulation. The comparison of the temperature results shows a good agreement

between the experimental and the numerical data. The accuracy of the 2D model for higher mass fluxes cannot be properly assessed on basis of the experimental data generated using this setup. But the accuracy of the 2D model for the higher mass flow cases is expected to be accurate, due to less complexity in the flow calculation because of smaller buoyancy effects.

References

[1] A. Kruse, Supercritical water gasification, Biofuels, Bioproducts and Biorefining 2 (5) (2008) 415–437.
[2] Y. Matsumura, T. Minowa, B. Potic, S. Kersten, W. Prins, W. van Swaaij, B. van de Beld, D. Elliott, G. Neuenschwander, A. Kruse, et al., Biomass gasification in near- and super-critical water: status and prospects, Biomass and Bioenergy 29 (4) (2005) 269–292.
[3] W. Wagner, A. Kruse, Properties of Water and Steam: The Industrial Standard IAPWS-IF97 for the Thermodynamic Properties and Supplementary Equations for Other Properties: Tables Based on These Equations, Springer-Verlag, 1998.
[4] J. Sallevelt, J. Withag, E. Bramer, D. Brilman, G. Brem, One-dimensional model for heat transfer to a supercritical water flow in a tube, The Journal of Supercritical Fluids, Elsevier 68 (2012) 1–12.
[5] D. Wilcox, Turbulence Modeling for CFD, DCW Industries, Inc, La Canada, CA, 1993.
[6] J. Jackson, M. Cotton, B. Axcell, Studies of mixed convection in vertical tubes, International Journal of Heat and Fluid Flow 10 (1) (1989) 2–15.
[7] R. Bird, W. Stewart, E. Lightfoot, Transport Phenomena, John Wiley & Sons, New York, 1960.
[8] E. Fares, W. Schroder, A differential equation for approximate wall distance, International Journal for Numerical Methods in Fluids 39 (8) (2002) 743–762.
[9] W. Kays, Turbulent Prandtl number. Where are we? ASME Transactions Journal of Heat Transfer 116 (1994) 284–295.
[10] H. Tanaka, S. Hatano, S. Maruyama, Combined forced and natural convection heat transfer for upward flow in a uniformly heated vertical pipe: Series b: Fluids engineering, heat transfer, combustion, power, thermophysical properties, JSME International Journal: Bulletin of the JSME 30 (266) (1987) 1348.
[11] J. Licht, M. Anderson, M. Corradini, Heat transfer to water at supercritical pressures in a circular and square annular flow geometry, International Journal of Heat and Fluid Flow 29 (1) (2008) 156–166.
[12] S. Mokry, I. Pioro, A. Farah, K. King, S. Gupta, W. Peiman, P. Kirillov, Development of supercritical water heat-transfer correlation for vertical bare tubes, Nuclear Engineering and Design 241 (4) (2011) 1126–1136.
[13] K. Yamagata, K. Nishikawa, S. Hasegawa, T. Fujii, S. Yoshida, Forced convective heat transfer to supercritical water flowing in tubes, International Journal of Heat and Mass Transfer 15 (12) (1972) 2575–2593.
[14] S. Mokry, I. Pioro, A. Farah, K. King, S. Gupta, W. Peiman, P. Kirillov, Development of supercritical water heat-transfer correlation for vertical bare tubes, Nuclear Engineering and Design, Elsevier 240 (3) (2010) 568–576.
[15] J. Jackson, W. Hall, Influences of buoyancy on heat transfer to fluids flowing in vertical tubes under turbulent conditions, Turbulent Forced Convection in Channels and Bundles 2 (1979) 613–640.
[16] T. Aicher, H. Martin, New correlations for mixed turbulent natural and forced convection heat transfer in vertical tubes, International Journal of Heat and Mass Transfer 40 (15) (1997) 3617–3626.
[17] J. Yu, B. Jia, D. Wu, D. Wang, Optimization of heat transfer coefficient correlation at supercritical pressure using genetic algorithms, Heat and Mass Transfer 45 (6) (2009) 757–766.
[18] H. Swenson, J. Carver, C. Kakarala, Heat transfer to supercritical water in smooth-bore tubes, Journal of Heat Transfer, Transactions of ASME, Series C 87 (4) (1965) 477–484.